Axion insulator states in a topological insulator proximitized to magnetic insulators: A tight-binding characterization

Mohammad Shafiei,[1,2] Farhad Fazileh,[1,*] François M. Peeters,[2] and Milorad V. Milošević[2,†]

[1]*Department of Physics, Isfahan University of Technology, Isfahan 84156-83111, Iran*
[2]*Department of Physics, University of Antwerp, Groenenborgerlaan 171, B-2020 Antwerp, Belgium*

The recent discovery of axion states in materials such as antiferromagnetic topological insulators has boosted investigations of the magnetoelectric response in topological insulators and their promise towards realizing dissipationless topological electronics. In this paper, we develop a tight-binding methodology to explore the emergence of axion states in Bi_2Se_3 in proximity to magnetic insulators on the top and bottom surfaces. The topological protection of the surface states is lifted by a time-reversal-breaking perturbation due to the proximity of a magnetic insulator, and a gap is opened on the surfaces, giving rise to half-quantized Hall conductance and a zero Hall plateau—evidencing an axion insulator state. We developed a real-space tight-binding Hamiltonian for Bi_2Se_3 using first-principles data. Transport properties of the system were obtained within the Landauer-Büttiker formalism, and we discuss the creation of axion states through Hall conductance and a zero Hall plateau at the surfaces, as a function of proximitized magnetization and corresponding potentials at the surfaces, as well as the thickness of the topological insulator.

I. INTRODUCTION

Axions are hypothetical particles introduced 40 years ago in quantum field theory, to solve the strong charge-parity problem in high-energy physics. However, observation in nature has evaded researchers to date [1]. Many particles discovered or hypothesized in particle physics to resolve a certain contradiction are found by analogy as quasiparticle excitations in condensed matter physics, such as massless Weyl fermions, Dirac fermions, and Majorana fermions, to name a few [2]. Axions are not an exception: Weakly interacting quasiparticles in materials such as antiferromagnetic topological insulators (AFM TIs) were shown to exhibit a governing dynamics that is similar to that of axion particles in high-energy physics [3,4]. Furthermore, the θ term in the topological magnetoelectric effect (TME) was shown to have the same form as the action describing the coupling between an axion particle and a photon [5]. The appearance of axion states in condensed matter systems is accompanied by several interesting phenomena such as the half-quantized anomalous Hall effect (QAHE) and the linear magnetoelectric response [1].

Subsequent studies in particle physics and astrophysics indicated that axions are candidates for dark matter. Identification of such dark axions is a challenging task due to their weak interaction with ordinary materials. Recently, it was proposed that topological insulators with a dynamical axion field can be utilized to detect dark axions, with theoretical prediction of the mass of these particles of 0.7–3.5 meV [6].

Therefore condensed matter systems based on topological insulators that can host axion quasiparticles—dubbed axion insulators (AIs)—are of prime scientific interest. Several works on axion states in the magnetic topological insulator $MnBi_2Te_4$ have recently been reported in the literature [7–10]. They develop an effective continuum Hamiltonian close to the Γ point and then approximate the original tight-binding Hamiltonian for low energies before discretizing the continuum Hamiltonian on a cubic lattice. In doing so, they do not address effects related to the symmetry of the structure or higher-energy outcomes. However, the performance of these materials can likely be exceeded by a suitable design of ferromagnet-TI heterostructures. In such heterostructures, magnetization and surface states can be tailored individually as they belong to different constituent materials, to achieve controllable and stable performance even at room temperature. This is the main objective of our theoretical investigation in this paper. The axion insulators are characterized by a half-quantized Hall conductance with opposite sign and chiral currents on the surfaces, the latter being clockwise and counterclockwise on opposite surfaces. The electromagnetic response of a three-dimensional insulator can be expressed by Maxwell's action [11,12]:

$$S = \frac{8}{\pi} \int d^3x \, dt \left(\varepsilon E^2 - \frac{1}{\mu} B^2 \right), \tag{1}$$

in which **E** and **B** are the electric and magnetic field inside the insulator and ε and μ represent the dielectric constant and the magnetic permeability, respectively. For insulators with broken time-reversal symmetry (TRS), spatial symmetry or a combination of spatial symmetry and TRS can lead to quantized θ. The axion term should be added to the action as

$$S_\theta = \frac{\theta}{2\pi} \frac{\alpha}{2\pi} \int d^3x \, dt \, \mathbf{E} \cdot \mathbf{B}, \tag{2}$$

*fazileh@cc.iut.ac.ir
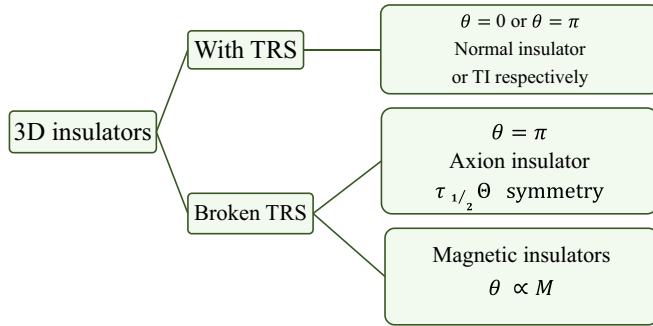†milorad.milosevic@uantwerpen.be

FIG. 1. Schematic classification of 3D insulators based on (broken) TRS and the axion term θ [5].

in which θ acts as an axion field. Here, $\alpha = e^2/\hbar c$ is the fine-structure constant. As $\mathbf{E} \cdot \mathbf{B}$ is odd under TRS, S_θ must be invariant when $\theta \to -\theta$. The axion field (θ) for time-reversal invariant insulators is quantized to 0 for normal insulators or π for strongly topological ones [1,13]. A schematic classification of TIs is depicted in Fig. 1 in terms of the existence or breaking of TRS. In the presence of TRS, $\theta = 0$ and $\theta = \pi$ correspond to normal insulators or TIs, respectively. For broken TRS, TI can be an axion insulator (AI) or a magnetic insulator. In an AI, although TRS is broken, a combination of TRS and lattice translation symmetry is conserved, which is known as effective TRS, and $\theta = \pi$. Magnetic insulators can have any arbitrary value of θ proportional to the magnetic order parameter M, i.e., $\theta(r, t) \propto \delta M(r, t)$ [5]. The axion term states that an electric field induces magnetic polarization and a magnetic field induces electric polarization. θ depends on the band structure of the insulator and can be expressed as follows [13]:

$$\theta = \frac{1}{4\pi} \int d^3k \, \epsilon^{ijk} \, \text{Tr}\left[A_i \, \partial_j A_k + i\frac{2}{3} A_i A_j A_k\right],$$

$$\text{with } A_j = -i\langle u_n | \frac{\partial}{\partial k_j} | u_m \rangle. \tag{3}$$

The topological magnetoelectric effect can be defined as a linear magnetoelectric polarization [13]:

$$\alpha_{ij} = \frac{\partial M_j}{\partial E_i}\bigg|_{B=0} = \frac{\partial P_i}{\partial B_j}\bigg|_{E=0} = \tilde{\alpha}_{ij} + \theta \frac{\alpha}{4\pi^2} \delta_{ij}, \tag{4}$$

where the tensor $\tilde{\alpha}_{ij}$ contains nine independent components for different contributions of spin, orbitals, and ions; for materials with inversion and time-reversal symmetry, $\tilde{\alpha}_{ij} = 0$. Here, we focus on magnetoelectric coupling resulting from the orbital magnetization and polarization. An axion insulator results in a TME in which an energy gap opens on the surfaces and the bulk quantization such that $\theta = \pi$. A gap is opened on the surfaces when surface states are broken by a time-reversal-breaking perturbation through an external magnetic field; if a TI is placed in proximity to a magnetic insulator; or in the presence of magnetic impurities on the three-dimensional (3D) TI surfaces. In such cases, the surface Hall conductivity becomes $\sigma_{xy} = \pm\frac{e^2}{2h}$, where the sign depends on the specific time-reversal-breaking perturbation [14,15]. If the direction of magnetization of the ferromagnetic (FM) materials which is in proximity to the TI is the same, the quantum Hall conductance

is half quantized, and $\sigma_{xy} = +\frac{e^2}{2h}$ for the top and bottom surfaces; therefore a chiral current emerges at the TI surfaces. For different directions of magnetization on the top and bottom surfaces, $\sigma_{xy} = \pm\frac{e^2}{2h}$ changes sign at surfaces, with no Hall current [16,17].

Some applications of axion insulators include antiferromagnetic topological insulators and their axion polaritons to detect dark matter, fabrication of nonreciprocal thermal emitters by Weyl semimetals, and detection of Majorana fermions in quantum anomalous Hall materials for topological quantum computing [1]. Faster advances in this field require the development of an efficient and convenient theoretical methodology to design and characterize the axion states in hybrid TI heterostructures, as well as detecting and examining these states at various energy scales. The latter is the ultimate objective of this paper, as exemplified through full characterization of axion insulator states in a ferromagnet-Bi_2Se_3-ferromagnet heterostructure after developing the tight-binding Hamiltonian for Bi_2Se_3 with the proximity effect included using the Zeeman term. We are dealing with a three-dimensional system, where developing a tight-binding model is challenging. We started from the microscopic scale and used density functional theory (DFT) data to fit a real-space Hamiltonian with the obtained band structure. Although this model is an effective one, it is well suited to capture experimental results such as the hybridization gap.

The paper is organized as follows. In Sec. II, we employ the symmetries to present the real-space Hamiltonian based on the parameters of the four-band Hamiltonian for Bi_2Se_3. In Sec. III, the effects of finite thickness and the hybridization gap are considered. The hybridization effect is calculated, and the proximity effect on the surface states is detailed. In Sec. IV, we develop the transport methodology and exemplify its use to characterize axion states in a Bi_2Se_3 proximitized to magnetic insulators, by calculating the longitudinal, transverse, and Hall conductance as well as the axion term θ. Section V summarizes our results and presents our conclusions.

II. THE MODEL HAMILTONIAN

The Bi_2Se_3 family of materials possess a rhombohedral crystal structure with the symmetry group D_{3d}^5 ($R\bar{3}m$) [18], as shown in Fig. 2. In the layered structure of Bi_2Se_3, atoms in layers are stacked along the z direction in an ABCABC sequence, with five layers in the unit cell; these five atomic layers are therefore usually referred to as a quintuple layer (QL) [19–21]. Each lattice site has six nearest neighbors in each layer and six next-nearest neighbors in adjacent layers. The vectors $\mathbf{a_i}$ to connect sites within each layer and vectors $\mathbf{b_i}$ to connect sites to adjacent layers can be written as [20] $\mathbf{a_1} = (a, 0, 0)$, $\mathbf{a_2} = (-a/2, a\sqrt{3}/2, 0)$, $\mathbf{a_3} = (-a/2, -a\sqrt{3}/2, 0)$, $\mathbf{b_1} = (0, \sqrt{3}a/3, c)$, $\mathbf{b_2} = (-a/2, -\sqrt{3}a/6, c)$, and $\mathbf{b_3} = (a/2, \sqrt{3}a/2, c)$. The ruling structural symmetries are as follows [18,20,21].

(i) The three-rotational symmetry around the z axis is given by $R_3 = \exp[((i\sigma_3 \otimes 1)/2)\theta]$, $\theta = 2\pi/3$.

(ii) The two-rotational symmetry around the x axis is given by $R_2 = [(i\sigma_2 \otimes \tau_3)]$.

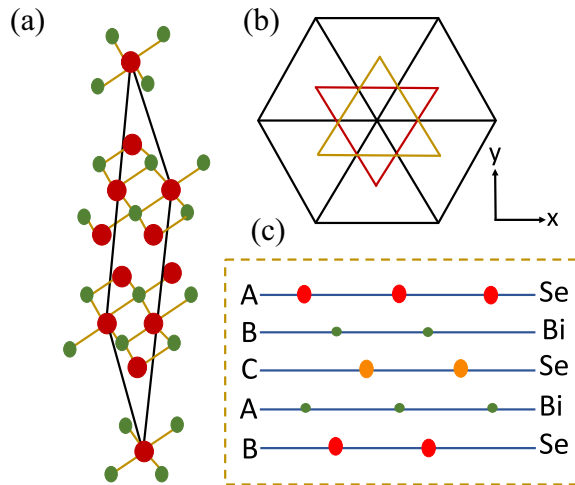(iii) The inversion symmetry is given by $P = 1 \otimes \tau_3$.

FIG. 2. (a) Bi_2Se_3 crystal structure. (b) Top view of atomic sites. (c) The atoms are stacked in layers in the z direction in an ABCABC sequence.
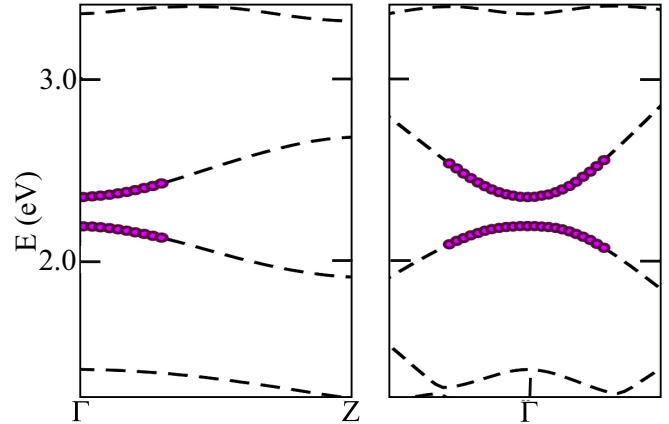

FIG. 3. Band structure of Bi_2Se_3 near the Γ point. Dashed lines represent DFT data, and filled circles show the band structure from the four-band Hamiltonian with fitted parameters near the Γ point.

(iv) The time-reversal symmetry is given by $T = (i\sigma_2 \otimes 1)K$, where K is a complex-conjugate operator and σ and τ are spin and pseudospin Pauli matrices.

D_{3d} is the direct multiplication of the D_3 group and the inverse operator group. Therefore group D_3 with spatial inversion and time-reversal eigenvalues is considered [18].

Table I represents polynomials of **k** and the Γ matrices under the transformations of the group D_3, inversion, and time reversal. By considering the irreducible representation, a four-band Hamiltonian was written as follows [21]:

$$H = \varepsilon_k' \otimes I + \begin{pmatrix} M_k' & A_1'k_z & 0 & A_2'k_- \\ A_1'k_z & -M_k' & A_2'k_- & 0 \\ 0 & A_2'k_+ & M_k' & -A_1'k_z \\ A_2'k_+ & 0 & -A_1'k_z & -M_k' \end{pmatrix}, \quad (5)$$

where $\varepsilon_k' = C_0' + C_1'k_z^2 + C_2'k_\perp^2, M_k' = M_0' + M_1'k_z^2 + M_2'k_\perp^2$ and $k_\perp^2 = k_x^2 + k_y^2$. By fitting the band structure obtained from this Hamiltonian with the band structure determined from DFT [22] (Fig. 3), we obtain $A_0' = 5.35$ eV Å, $B_0' = 4.44$ eV Å, $C_0' = -0.0063$ eV Å, $C_1' = 6.65$ eV Å^2, $C_2' = -1.75$ eV Å^2, $M_0' = 0.29$ eV Å^2, $M_1' = -10.25$ eV Å^2, and $M_2' = -56.6$ eV Å^2, which are similar to the values found in the work of Liu *et al.* [21]. In this section, a real-space

TABLE I. Polynomials of **k** and the Γ matrices under the transformations of the group D_3, inversion, and time-reversal symmetry. $\Gamma_5 = \sigma_0 \otimes \tau_3$, and $\Gamma^{(1)}$, $\Gamma^{(2)}$, and $\Gamma^{(3)}$ are irreducible representations of group D_3. **k** polynomials can only exist in the Hamiltonian according to the irreducible representations of group D_3, as given in the table. Dim, dimension.

T	P	$\Gamma^{(1)}$ (Dim = 1)	$\Gamma^{(2)}$ (Dim = 2)	$\Gamma^{(3)}$ (Dim = 3)
+	+	$\{k_z^2\}$		$\{ik_zk_+, -ik_zk_-\}$
		$\{k_\perp\}$		$\{k_-^2, k_+^2\}$
		Γ_5		

tight-binding Hamiltonian is constructed whose hopping parameters are related to the parameters of the effective four-band Hamiltonian near the Γ point, introduced by Chu *et al.* [23]. It should also be emphasized that, even though we are dealing with an effective tight-binding model, other effects such as gate voltage, electric field, magnetic field, and strain can be straightforwardly added to the consideration based on the symmetry group of the system. To construct a tight-binding Hamiltonian, each unit cell was considered to contain two atoms (Bi and Se) and spin, giving rise to four states for each unit cell. We considered only the hopping between nearest neighbors. Figure 4 depicts the structure of Bi_2Se_3 in the x-y plane. Considering the nearest neighbors only, each unit cell will have six neighboring unit cells in the x-y plane that are connected by vectors $\mathbf{n_i}$ ($\mathbf{i = 1, 2, 3}$) and two unit cells in the z direction connected by vector $\mathbf{n_4}$. The real-space Hamiltonian is written as follows [10,23]:

$$H = \Sigma_i c_i^\dagger E_{on} c_i + \Sigma_{i,\alpha}(c_i^\dagger T_\alpha c_{i+\alpha} + \text{H.c.}), \quad (6)$$
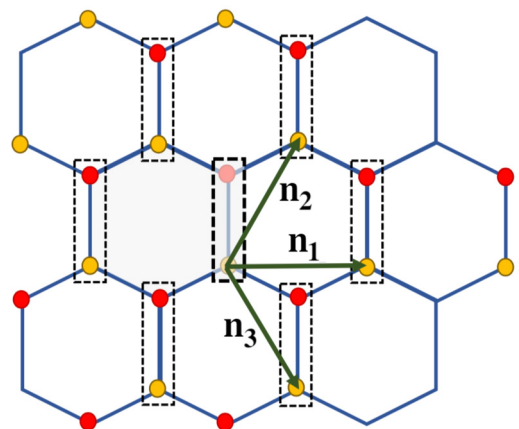

FIG. 4. Lattice structure of Bi_2Se_3 in the x-y plane. Each unit cell has six neighboring unit cells in the x-y plane that are connected by vectors $\mathbf{n_i}$ ($\mathbf{i = 1, 2, 3}$) and two unit cells in the z direction that are connected by vector $\mathbf{n_4}$.

TABLE II. Hybridization gap due to finite-size effect. The values in the first row are obtained from our model, and the values in the second row are from Ref. [25].

	Hybridization gap (eV)			
	Two QLs	Three QLs	Four QLs	Five QLs
Our model	0.257	0.118	0.057	0.028
Ref. [25]	0.252	0.138	0.070	0.041

where $\alpha = \mathbf{n_1}, \mathbf{n_2}, \mathbf{n_3}, \mathbf{n_4}$ and the operator $c_i^\dagger$ (c_i) creates (annihilates) an electron at site i. Furthermore, we have

$$E_{\text{on}} = (E_0 - 2\Sigma_\alpha B_\alpha)\sigma_z \otimes \sigma_0 \qquad (7)$$

and

$$T_\alpha = C_\alpha \sigma_0 \otimes \sigma_0 + B_\alpha \sigma_z \otimes \sigma_0 - i\left(\frac{A_\alpha}{2}\right)\sigma_x \otimes \sigma \cdot \mathbf{n}_\alpha. \qquad (8)$$

E_{on} and T_α are 4×4 matrices corresponding to the hopping parameters and stand for on-site energy and hopping parameters between unit cells, respectively. Based on the structure of the system, $\mathbf{n_1} = (1/2, \sqrt{3}/2, 0)$, $\mathbf{n_2} = (-1/2, \sqrt{3}/2, 0)$, $\mathbf{n_3} = (1, 0, 0)$, and $\mathbf{n_4} = (0, 0, 1)$. Because of the symmetries of the system, A_{n_1,n_2,n_3}, B_{n_1,n_2,n_3}, and C_{n_1,n_2,n_3}, which are related to the x-y plane parameters, are isotropic, and therefore we use the notation $A_{n_1,n_2,n_3} = A_2$, $B_{n_1,n_2,n_3} = B_2$, $C_{n_1,n_2,n_3} = C_2$, while for n_4 parameters we take $A_{n_4} = A_1$, $B_{n_4} = B_1$, and $C_{n_4} = C_1$. By matching this Hamiltonian with the four-band Hamiltonian near the Γ point, i.e., for $k \to 0$, the parameters of the tight-binding Hamiltonian can be determined.

III. FINITE-SIZE AND PROXIMITY EFFECTS ON SURFACE STATES

The Bi$_2$Se$_3$ surface Hamiltonian in the basis of the top and bottom states with spin $\uparrow$, $\downarrow$ $\{t \uparrow, t \downarrow, b \uparrow, b \downarrow\}$ can be written as follows [11,24]:

$$H_{\text{surf}}(k_x, k_y) = \hbar v_F(k_y\sigma_x - k_x\sigma_y) \otimes \sigma_z + \Delta_m\sigma_0 \otimes \sigma_x, \qquad (9)$$

where v_F is the Fermi velocity, $\Delta_m = \Delta_h + Bk^2$ represents the coupling between the top and bottom states, and Δ_h denotes the coupling gap at the surfaces [25,26]. In the three-dimensional topological insulator family of Bi$_2$Se$_3$, the bulk samples have a gap, while the surface states are gapless and contain a Dirac cone. When the thickness of the sample is reduced to nanoscale, there will be an overlap between the wave functions of the top and bottom surface states, and the spin-polarized surface states of one surface combine with the opposite-spin components on the other surface, resulting in a gap at the Dirac point. Here, the penetration depth was determined for surface states considering the eigenfunctions of surface states. Then, the hybridization gap was calculated for surface states in several layers along the z direction. The obtained hybridization gap due to the finite-size effect is shown in Fig. 5 and Table II and is consistent with experimental results [25] and DFT data [11]. One concludes that to prevent surface hybridization, the thickness of the sample should be at least six QLs. As mentioned earlier, to investigate the effect of magnetization on the surface states, instead
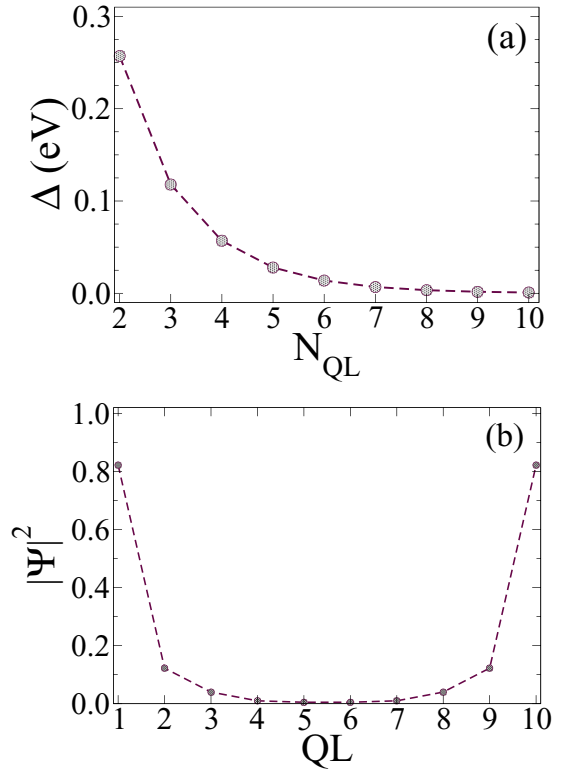

FIG. 5. (a) Hybridization gap due to the finite-size effect on the surface states, as a function of TI thickness [expressed as the number of quintuple layers (QLs)]. (b) Penetration of surface state wave function into the bulk, for a ten-QL-thick sample.

of using a two-dimensional effective surface Hamiltonian, a three-dimensional effective Hamiltonian was employed in real space. Concerning a 2D model, the proximitized magnetization (weak Zeeman field) leads to gaps in the Dirac cones on the surfaces. For a 3D model, however, the application of magnetization results in the formation of a gap in the Dirac cones on the top and bottom surfaces, while the side surfaces remain gapless [23]. Figure 6 illustrates the band structure and gapless single Dirac cone of the surface states at the Γ point. Applying the Zeeman splitting term introduces a gap.

The magnetization effect on the top and bottom surfaces can be achieved in two different ways: (i) by doping with magnetic atoms (inclusions) on the top and bottom surfaces or (ii) by proximitized magnetic material near those surfaces. Magnetic materials to impose magnetization on the surface states of the TI must be able to establish strong magnetic coupling at the interface while causing no effect on states near the Fermi energy [27]. Magnetization can be added to the Hamiltonian by the Zeeman term:

$$H_{\text{Zeeman}} = \Delta_{t/b}\sigma_0 \otimes \sigma_z, \qquad (10)$$

where Δ_t and Δ_b are the exchange fields and represent the gaps opening due to the magnetization applied to the topological surface states in the top and bottom surfaces, respectively [14,28]. For different magnitudes of the magnetizations on the top and bottom surfaces, the Zeeman term and the gap on the top and bottom surfaces will also be different. Thus a term related to structural inversion asymmetry (SIA)
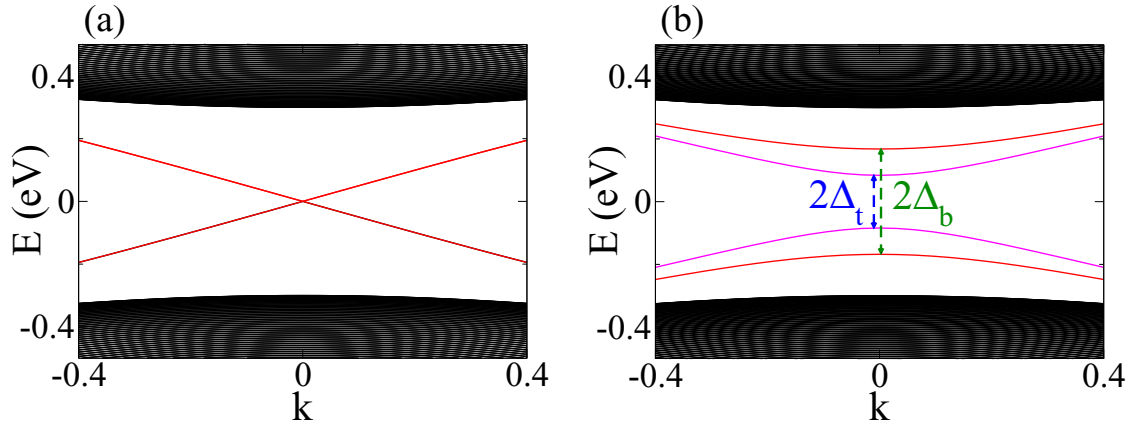
FIG. 6. (a) The band structure and the gapless Dirac cone of the surface states at the Γ point. (b) Applying the Zeeman splitting term causes a gap to open; here, $\Delta_t = 0.1$ eV and $\Delta_b = -0.2$ eV.

should be added [11,24]. This term is a potential difference between two surfaces (V_{sia}) and splits each spin-degenerate band into two subbands. Figure 7 presents the effect of magnetization and structural inversion asymmetry on TI surface states with a single Dirac cone. Magnetization opens a gap in the Dirac point while V_{sia} tunes the dispersion bands in different directions. The following term should be added to the Hamiltonian:

$$H_{sia} = V_{sia}\sigma_0 \otimes \sigma_z. \quad (11)$$

IV. AXION INSULATOR STATES IN THE FM-Bi$_2$Se$_3$-FM HETEROSTRUCTURE

In what follows, the FM-TI-FM heterostructure shown in Fig. 8 is used to study the emergent axion states and the topological magnetoelectric effect. The essential condition for

the topological magnetoelectric effect is lost in the presence of hybridization between the top and bottom surface states. Therefore the topological insulator should be sufficiently thick to guarantee the absence of hybridization between the top and bottom states [30]. As discussed in the previous section, in the case of Bi$_2$Se$_3$ the minimum number of quintuple layers to consider is 7. In addition, the exchange fields due to the magnetization applied to the topological insulator at the top and bottom surfaces should have opposite sign (i.e., $\Delta_t\Delta_b < 0$) [11,31]. One of the challenges in the fabrication of heterostructures to observe axion states is the proper choice of materials that will be used in the proximity of 3D TIs. In addition to structural and magnetic stability, these heterostructures must exhibit a robust spin-polarized band gap in the interface states. A sufficient selection of thin magnetic insulators is nowadays experimentally accessible to sandwich a TI for the purpose of creating axion states, such as CrI$_3$, Cr$_2$Ge$_2$Te$_6$, MnBi$_2$Se$_4$, and MnBi$_2$Te$_4$ [32,33]. For example, for opposite magnetization of the two magnetic layers in a CrI$_3$-Bi$_2$Se$_3$-MnBi$_2$Se$_4$ heterostructure, $\Delta_t = 3.2$ meV, $\Delta_b = -26.9$ meV, and $V_{sia} = 9.35$ meV at the Bi$_2$Se$_3$ surfaces [11]. A zero Hall plateau and $\theta = \pi$ are then the main signatures of the axion state. For characterization of transport or conductance, in this section we consider a four-terminal
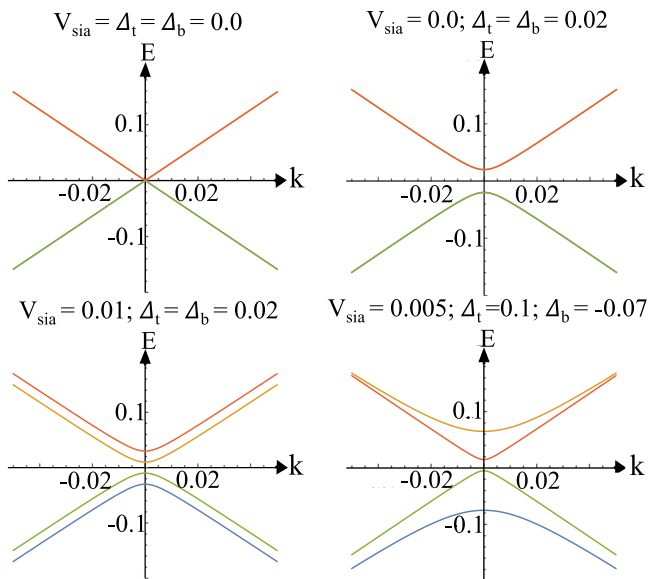

FIG. 7. Effect of magnetization and of structural inversion asymmetry on surface states for different V_{sia}, Δ_t, and Δ_b (in eV).
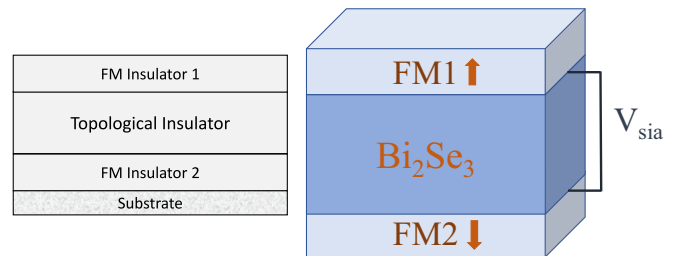

FIG. 8. FM-Bi$_2$Se$_3$-FM heterostructure with opposite polarity of magnetization at the two surfaces of the TI. In such a case, the half-quantized Hall conductance will have different sign at the surfaces, and the net Hall conductance becomes zero [29]. Theoretical consideration of the finite thickness of the TI requires additional potential (V_{sia}) to capture the physics due to the structural inversion asymmetry.
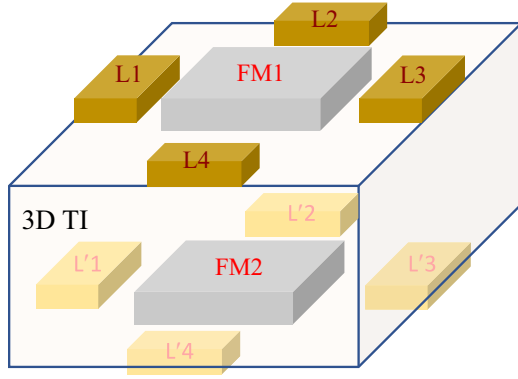
FIG. 9. Schematic illustration of the 3D device with 2D leads to measure the longitudinal (σ_{xx}) and Hall conductance (σ_{xy}) at the surface.
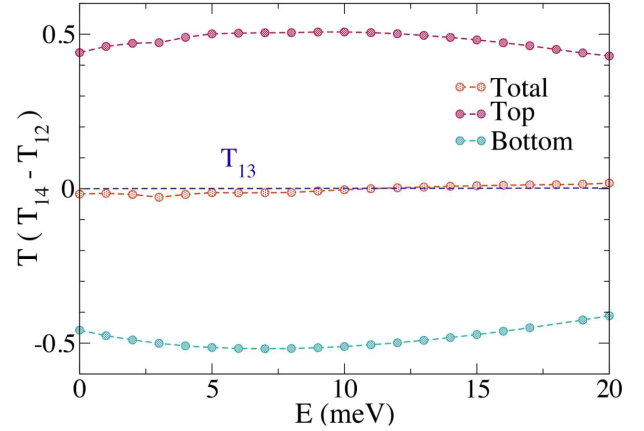

FIG. 10. Hall transmission coefficient for the top and bottom surfaces separately and the total Hall conductance, for $\Delta_t = 5$ meV and $\Delta_b = -25$ meV.

sample as depicted in Fig. 9. The longitudinal conductance (σ_{xx}) and Hall conductance (σ_{xy}) were calculated using the Landauer-Büttiker formalism. This formalism treats conductance in terms of the transmission coefficients of the device. The transmission coefficient between leads i and j can be determined in terms of Green's functions as [34]

$$T_{ij} = \text{tr}[\Gamma_i G_{ij} \Gamma_j G_{ij}^\dagger], \qquad (12)$$

where Γ_i describes the coupling of the device to the leads and can be expressed in terms of a self-energy Σ_i as $\Gamma_i = i[\Sigma_i - \Sigma_i^\dagger]$. Here, Σ_i can be considered as an effective Hamiltonian describing the lead-device interaction [35]. The Hamiltonian of the complete system can be subdivided as follows:

$$H = H_D + \sum_i (H_L^i + V_{LD}^i + V_{DL}^i), \qquad (13)$$

where H_D denotes the device Hamiltonian, H_L^i is the Hamiltonian for the ith lead, and V_{LD}^i and V_{DL}^i denote the left and right Hamiltonian between the ith lead and device, respectively. In this setup, four identical semi-infinite leads are attached to the sample, and the longitudinal and Hall conductances are given by [36]

$$\sigma_{xx} = \frac{e^2}{2h} T_{13}, \quad \sigma_{xy} = \frac{e^2}{2h}(T_{14} - T_{12}). \qquad (14)$$

A prerequisite for AI states is that the values of Δ_t and Δ_b at the surfaces have opposite sign. The localization of the Hall conductance on the surfaces weakly depends on the Zeeman terms as the magnitude of Δ_t and Δ_b increases, but we use 2D leads to calculate the Hall conductance; thus the amount of this conductance does not vary [37]. As explained previously, the Hall conductance is weakly dependent on the Zeeman term chosen; thus we use $\Delta_t = 5$ meV and $\Delta_b = -25$ meV. Our calculated longitudinal and Hall conductances are shown in Fig. 10 for the system with $\Delta_t = 5$ meV and $\Delta_b = -25$ meV. A half-quantized Hall conductance appears upon applying the magnetization to the top and bottom surfaces of a TI due to the configuration of the structure and can be formulated as [11,24]

$$\sigma_{xy}^{t/b} = \text{sgn}(\Delta_{t/b})\frac{e^2}{2h}. \qquad (15)$$

It should be noted that calculating or measuring the half quantization for each surface independently is challenging. As a qualitative indication, Chen *et al.* [10] recently proposed a nonlocal surface transport device in which the axion insulator can be distinguished from normal insulators without a precise measurement of the half quantization. Instead, we calculate the Hall conductance for the top and bottom surfaces separately as a more definite proof of the axion insulator states. Going beyond the previous work [7–10], our calculations are more challenging, but the results are exceedingly more accurate. For calculation of the quantum transport in this system we employed an original tight-binding Hamiltonian obtained from symmetry considerations and *ab initio* calculations, which was a nontrivial task as we had to construct the Landauer-Büttiker formulation for the complex crystal structure of this system.

When the magnetic materials adjacent to the TI are different, a V_{sia} needs to be applied to the top and bottom surfaces of the TI. As discussed also in Ref. [11], V_{sia} causes a phase transition from the axion insulator state to the metallic state as the band gap closes with increasing value of V_{sia}. We refer to the minimum band gap that is induced by the Zeeman terms ($\min\{\Delta_t, \Delta_b\}$) as the magnetization gap. Based on Fig. 11, when V_{sia} ranges between 0 and $|\Delta_t - \Delta_b|/2$ (0–10 meV in the case considered in Fig. 11), the magnetization band gap is 10 meV, and for V_{sia} values between $||\Delta_t| - |\Delta_b||/2$ and $||\Delta_t| + |\Delta_b||/2$ (10–15 meV), the band gap linearly decreases. For V_{sia} values above $||\Delta_t| + |\Delta_b||/2$ (15 meV), the band gap tends to zero, giving rise to a metallic state. One has axion states as long as the value of V_{sia} is between 0 and $||\Delta_t| + |\Delta_b||/2$. V_{sia} can only change the size of the magnetization gap, but since we consider E inside the band gap to calculate the conductance, the Hall conductance is independent of V_{sia}. For the same direction of magnetization at the top and the bottom surface we have $\sigma_{xy} = (C_t + C_b)\frac{e^2}{h} = \frac{e^2}{h}$, and if the magnetizations have opposite direction, $\sigma_{xy} = 0$ [38]. The latter can characterize two different modes, i.e., either the axion insulator state or the normal insulator state [10]. To determine whether $\sigma_{xy} = 0$ corresponds to the axion insulator or the normal insulator, the electrical transport needs to
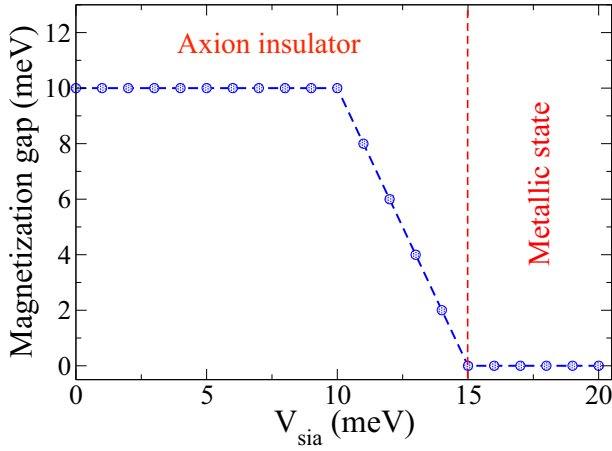
FIG. 11. Phase diagram as a function of V_{sia}. We took $\Delta_t = 5$ meV and $\Delta_b = -25$ meV and found that V_{sia} between 0 and 15 meV yields axion insulator states, while for $V_{sia} > 15$ meV one finds a metallic state (cf. Ref. [11]).

be calculated independently on the top and bottom surfaces using the Landauer-Büttiker formalism. For axion insulators, transport on the top and bottom surfaces is opposite and leads to net zero transport, while for normal insulators, transport is zero on both surfaces.

As stated in the Introduction, in magnetoelectric materials, the application of an electric field **E** induces magnetization **M**, and the application of a magnetic field **B** induces polarization **P**. For 3D insulators, a classification based on TRS and magnetoelectric coupling θ can be introduced. When TRS is broken, the insulators are further subdivided into two categories. If TRS is broken but there is a symmetry as a sum of TRS and translational symmetry (dubbed effective TRS), one deals with an axion insulator, and in this case $\theta = \pi$ [3,5]. As shown in Fig. 12, we calculated the axion term θ for the FM-TI-FM heterostructure as a function of the TI thickness (in units of quintuple layers). With increasing
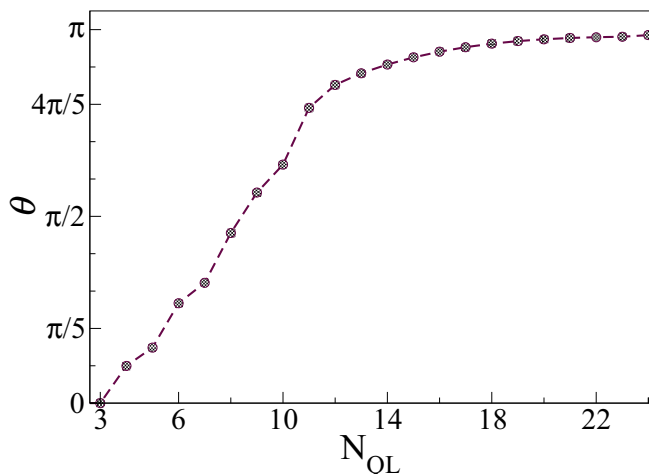

FIG. 12. The axion term θ for different TI thicknesses (numbers of QLs) in the case of $\Delta_t = 5$ meV, $\Delta_b = -25$ meV, and $V_{sia} = 0$. With increasing thickness, $\theta \to \pi$, characterizing the formation of an axion insulator state for thicknesses beyond ten QLs.

number of QLs, $\theta \to \pi$, indicating the formation of an axion insulator for $N_z > 10$ (for other parameters, $\Delta_t = 5$ meV, $\Delta_b = -25$ meV, and $V_{sia} = 0$). A moderate electric field can be considered as an on-site energy varying linearly from the bottom to the top of the TI film, such that magnetization becomes linearly dependent on the electric field and the axion angle θ can be computed.

V. CONCLUSIONS

In summary, we developed a real-space tight-binding Hamiltonian for Bi_2Se_3 taking into account the symmetry of the system and fitting the parameters using the band structure obtained from DFT. This derived tight-binding model is the most important aspect of our study. We show that it is readily well suited to capture experimental results such as the hybridization gap, but the effects of gating, magnetic field, and strain can also be relatively straightforwardly added to the consideration in our model based on the symmetry group of the system. Since this model is represented in real space, further studies of the effects of doping and magnetic and nonmagnetic impurities are facilitated.

In this paper, we went on to apply the developed model to a TI sandwiched between magnetic insulators, where the magnetic proximity effect was added through the Zeeman term to create favorable conditions for the appearance of the axion insulator states. In cases when different magnetic materials are considered, that induce exchange fields of opposite sign at their interfaces with the TI, a potential difference due to structural inversion asymmetry V_{sia} was taken into account between the top and bottom surfaces of the TI. In doing so, we demonstrated that a phase transition from the axion state to the metallic state occurs with increasing V_{sia}. To further characterize the axion insulator state, a four-terminal structure was considered to calculate the longitudinal and Hall conductance using the Landauer-Büttiker formalism. The total Hall conductance of the axion insulator is expected to be zero; however, the same is expected from a trivial band insulator. Therefore, to distinguish between a normal insulator and an axion insulator, we performed the calculation of the Hall conductance for each surface separately, to identify the axion state. Furthermore, by calculating the axion term θ for a heterostructure in which a magnetization gap of opposite sign is induced at the top and bottom surfaces of the TI, we showed that by increasing the thickness of the TI beyond a threshold of 11 quintuple layers one reaches $\theta \approx \pi$—the characteristic feature of an axion insulator. These findings validate the simulation framework approach developed in this paper, set the key limits on the stability of the axion insulator state in FM-TI-FM heterostructures, and open a platform for further *in silico* tailoring of the magnetoelectric response in TI heterostructures by design.

[1] D. M. Nenno, C. A. Garcia, J. Gooth, C. Felser, and P. Narang, Nat. Rev. Phys. **2**, 682 (2020).

[2] H. Wang, D. Wang, Z. Yang, M. Shi, J. Ruan, D. Xing, J. Wang, and H. Zhang, Phys. Rev. B **101**, 081109(R) (2020).

[3] R. Li, J. Wang, X.-L. Qi, and S.-C. Zhang, Nat. Phys. **6**, 284 (2010).

[4] M. Mogi, M. Kawamura, R. Yoshimi, A. Tsukazaki, Y. Kozuka, N. Shirakawa, K. Takahashi, M. Kawasaki, and Y. Tokura, Nat. Mater. **16**, 516 (2017).

[5] A. Sekine and K. Nomura, J. Appl. Phys. **129**, 141101 (2021).

[6] D. J. Marsh, K. C. Fong, E. W. Lentz, L. Šmejkal, and M. N. Ali, Phys. Rev. Lett. **123**, 121601 (2019).

[7] J. Ge, Y. Liu, P. Wang, Z. Xu, J. Li, H. Li, Z. Yan, Y. Wu, Y. Xu, and J. Wang, Phys. Rev. B **105**, L201404 (2022).

[8] Z. Liu, D. Qian, Y. Jiang, and J. Wang, arXiv:2109.06178.

[9] Y.-H. Li and R. Cheng, Phys. Rev. Research **4**, L022067 (2022).

[10] R. Chen, S. Li, H.-P. Sun, Q. Liu, Y. Zhao, H.-Z. Lu, and X. C. Xie, Phys. Rev. B **103**, L241409 (2021).

[11] Y. Hou, J. Kim, and R. Wu, Phys. Rev. B **101**, 121401(R) (2020).

[12] X.-L. Qi and S.-C. Zhang, Rev. Mod. Phys. **83**, 1057 (2011).

[13] A. M. Essin, J. E. Moore, and D. Vanderbilt, Phys. Rev. Lett. **102**, 146805 (2009).

[14] X.-L. Qi, T. L. Hughes, and S.-C. Zhang, Phys. Rev. B **78**, 195424 (2008).

[15] K. Nomura and N. Nagaosa, Phys. Rev. Lett. **106**, 166802 (2011).

[16] J. Wang, B. Lian, and S.-C. Zhang, Phys. Rev. B **93**, 045115 (2016).

[17] T. Morimoto, A. Furusaki, and N. Nagaosa, Phys. Rev. B **92**, 085113 (2015).

[18] M. R. Brems, J. Paaske, A. M. Lunde, and M. Willatzen, New J. Phys. **20**, 053041 (2018).

[19] H. Zhang, C.-X. Liu, X.-L. Qi, X. Dai, Z. Fang, and S.-C. Zhang, Nat. Phys. **5**, 438 (2009).

[20] S. Mao, A. Yamakage, and Y. Kuramoto, Phys. Rev. B **84**, 115413 (2011).

[21] C.-X. Liu, X.-L. Qi, H. Zhang, X. Dai, Z. Fang, and S.-C. Zhang, Phys. Rev. B **82**, 045122 (2010).

[22] I. Aguilera, C. Friedrich, and S. Blügel, Phys. Rev. B **100**, 155147 (2019).

[23] R.-L. Chu, J. Shi, and S.-Q. Shen, Phys. Rev. B **84**, 085312 (2011).

[24] Y. Hou and R. Wu, Nano Lett. **19**, 2472 (2019).

[25] Y. Zhang, K. He, C.-Z. Chang, C.-L. Song, L.-L. Wang, X. Chen, J.-F. Jia, Z. Fang, X. Dai, W.-Y. Shan, S.-Q. Shen, Q. Niu, X.-L. Qi, S.-C. Zhang, X.-C. Ma, and Q.-K. Xue, Nat. Phys. **6**, 584 (2010).

[26] A. Sabzalipour, M. Mir, M. Zarenia, and B. Partoens, J. Phys.: Condens. Matter **33**, 325702 (2021).

[27] H. Fu, C.-X. Liu, and B. Yan, Sci. Adv. **6**, eaaz0948 (2020).

[28] J. Zhang, Z. Liu, and J. Wang, Phys. Rev. B **100**, 165117 (2019).

[29] C.-X. Liu, S.-C. Zhang, and X.-L. Qi, Annu. Rev. Condens. Matter Phys. **7**, 301 (2016).

[30] K. M. Fijalkowski, N. Liu, M. Hartl, M. Winnerlein, P. Mandal, A. Coschizza, A. Fothergill, S. Grauer, S. Schreyeck, K. Brunner, M. Greiter, R. Thomale, C. Gould, and L. W. Molenkamp, Phys. Rev. B **103**, 235111 (2021).

[31] J. Wang, B. Lian, X.-L. Qi, and S.-C. Zhang, Phys. Rev. B **92**, 081107(R) (2015).

[32] C. Gong, L. Li, Z. Li, H. Ji, A. Stern, Y. Xia, T. Cao, W. Bao, C. Wang, Y. Wang, Z. Q. Qiu, R. J. Cava, S. G. Louie, J. Xia, and X. Zhang, Nature (London) **546**, 265 (2017).

[33] B. Chen, F. Fei, D. Zhang, B. Zhang, W. Liu, S. Zhang, P. Wang, B. Wei, Y. Zhang, Z. Zuo, J. Guo, Q. Liu, Z. Wang, X. Wu, J. Zong, X. Xie, W. Chen, Z. Sun, S. Wang, Y. Zhang *et al.*, Nat. Commun. **10**, 4469 (2019).

[34] S. Datta, *Electronic Transport in Mesoscopic Systems* (Cambridge University Press, Cambridge, 1997).

[35] V. Nam Do, V. H. Nguyen, P. Dollfus, and A. Bournel, J. Appl. Phys. **104**, 063708 (2008).

[36] J. Li, L. Hu, and S.-Q. Shen, Phys. Rev. B **71**, 241305(R) (2005).

[37] N. Pournaghavi, A. Pertsova, A. MacDonald, and C. M. Canali, Phys. Rev. B **104**, L201102 (2021).

[38] H.-Z. Lu, W.-Y. Shan, W. Yao, Q. Niu, and S.-Q. Shen, Phys. Rev. B **81**, 115407 (2010).

Correction: A minor typographical error in the equation given in item (i) of the list below the first paragraph of Sec. II has been fixed.